

High-performing All-solid-state Sodium-ion Batteries Enabled by the Presodiation of Hard Carbon

Jin An Sam Oh,^{†1,2} Grayson Deysher,^{†3} Phillip Ridley,¹ Yu-Ting Chen,³ Diyi Cheng,¹ Ashley Cronk,³ So-Yeon Ham,³ Darren H.S. Tan,¹ Jihyun Jang,¹ Long Hoang Bao Nguyen,¹ and Ying Shirley Meng^{1,4,*}

¹Department of NanoEngineering, University of California San Diego, La Jolla, CA 92093, United States.

²Institute of Materials, Research, and Engineering, Agency of Science, Technology, and Research (A*STAR), Singapore

³Program of Materials Science and Engineering, University of California San Diego, La Jolla, CA 92093, United States.

⁴Pritzker School of Molecular Engineering, The University of Chicago, Chicago, IL 60637, United States

*Corresponding author: Ying Shirley Meng (Email: shirleymeng@uchicago.edu)

†Authors contributed equally.

All-solid-state sodium ion batteries (AS³iBs) are highly sought after for stationary energy storage systems due to their suitable safety and stability over a wide temperature range. Hard carbon (HC), which is low cost, exhibits a low redox potential, and a high capacity, is integral to achieve a practical large-scale sodium-ion battery. However, the energy density of the battery utilizing this anode material is hampered by its low initial Coulombic efficiency (ICE). Herein, two strategies, namely (i) thermal treatment and (ii) presodiation by thermal decomposition of NaBH₄, are explored to improve the ICE of pristine HC. Raman spectroscopy, X-ray photoelectron spectroscopy and electrochemical characterizations elucidate that the thermal treatment increases the C_{sp2} content in the HC structure, while the presodiation supplies the sodium to occupy the intrinsic irreversible sites. Consequently, presodiated HC exhibits an outstanding ICE (>99%) compared to the thermally treated (90%) or pristine HC (83%) in half-cell configurations. More importantly, AS³iB using presodiated HC and NaCrO₂ as the anode and cathode, respectively, exhibits a high ICE of 92% and an initial discharge energy density of 294 Wh kg⁻¹_{cathode}.

1. Introduction

Recent global electrification efforts have resulted in the price of lithium resources trending upwards and, thus, the cost of lithium-ion batteries (LIBs) to increase at an unprecedented rate.^[1] Due to the abundance and low cost of sodium-based materials, sodium-ion batteries (SIBs) can play an important role as a complementary system, especially in large-scale stationary energy storage systems.^[2] Conventional LIBs and SIBs use organic liquid electrolytes which then pose leakage risks, narrow temperature windows for operation, and are also flammable. Replacing the separator and liquid electrolyte with an inorganic solid-state electrolyte (SSE) can effectively mitigate the limitations of conventional batteries. In all-solid-state sodium ion batteries (AS³iBs), the electrochemical stability of the SSE with the electrode determines the type of interface.^[3] A thermodynamically stable interface between the SSE and the electrode is preferred to eradicate sodium loss due to formation of SEI. Recently, Na₄(B₁₀H₁₀)(B₁₂H₁₂), or NBH, SSE has been reported to have a high ionic conductivity around 1 mS cm⁻¹, which is very similar to common liquid electrolytes, allowing these AS³iBs to operate at room temperature with minimal overpotential.^[4] Moreover, it is electrochemically stable with metallic sodium allowing for a stable interface at low potential.^[5] Thus, NBH is a promising SSE which can be paired with the anode in the AS³iB.

Although numerous alloy-based materials, such as Sn, Sb, and Ge,^[6] have shown good potential as sodium anode materials, carbon-based materials are preferred for their environmental-friendliness, low cost, and low redox potentials. Hard carbon (HC), which consists of a low degree of graphitized carbon, has been shown to be a promising anode material for SIBs with a specific capacity of 250–300 mAh g⁻¹.^[7] Furthermore, HC exhibits low redox potential (~1 to 0.1 V vs. Na/Na⁺) that can theoretically enable high energy density batteries. However, the bottleneck that limits the application of HC in practical batteries is its low initial Coulombic efficiency (ICE).^[8] Consequently, the full-cell configuration, where a cathode provides mobile sodium ions inventory, suffers from poor reversibility and severely hinders the commercial potential.^[9] The loss of active sodium in the first cycle is primarily attributed to the formation of a solid electrolyte interphase (SEI) at the interface between HC and electrolyte.^[10] In addition to SEI formation, functional groups or surface defects within the HC structure, which possess high binding energies with

sodium ions, can also contribute to its low ICE.^[11] The presence of such Na irreversible sites can be greatly reduced by controlling the precursor sources, temperature, and annealing time.^[12] Nonetheless, these irreversible sites cannot be eliminated completely even when using optimal synthesis conditions. To overcome the low ICE, presodiating the HC is one of the most promising methods to compensate for the loss of mobile sodium ions inventory during the initial cycling.^[13] To date, presodiation has been achieved either electrochemically or chemically which inevitably creates an organic layer on the HC due to the decomposition of the organic electrolyte at the low potentials during presodiation.^[9a, 14]

In this study, two strategies are investigated to improve the ICE of the HC anode: (1) thermal treatment at 1000 °C and (2) presodiation by the thermal decomposition of NaBH₄ additive. The experimental results suggest that thermal treatment increases the C_{sp2}:C_{sp3} ratio, while the thermal decomposition of NaBH₄ produces metallic sodium on the HC surfaces to compensate sodium loss. Consequently, the thermally treated HC has an improved half-cell ICE, increasing from 83% to 90%, while presodiation enables an extremely high ICE of >99%. Electrochemical characterization and X-ray photoelectron spectroscopy reveals that the irreversible sodium ions in the HC exist in the form of Na–O–C, which is an intrinsic sodium storage mechanism in HC structure. Lastly, AS³iBs are assembled to demonstrate that the ICE can be increased from 75% to 92% and that the capacity retention is significantly higher by presodiating the HC.

2. Results and Discussion

The long-range structures of pristine hard carbon (HC), thermally treated hard carbon (HCT), and presodiated hard carbon (HCP) were investigated by X-ray diffraction (XRD). All three samples exhibited broad diffraction peaks (**Figure 1a**) indicating that all the samples have low crystallinity. **Table 1** summarizes the average interlayer spacing between graphene sheets (d_{002}), the average width of the order-layered nanodomains (L_a) and thickness (L_c) of the coherent domain, and the number of graphene sheets per stack (N) estimated by the Bragg's equation, Debye-Scherrer equation (**Equations 1 and 2**) and the XRD profiles.^[15] The estimated d_{002} of HC, HCT, and HCP were around 3.89, 3.86, and 4.01 Å, respectively, which are larger than that of graphite (~3.34 Å) and will be favorable for sodium ions insertion.^[15a, 16] Compared to pristine HC, the HCT exhibited a slight expansion in the L_c , L_a , and N which can be attributed to thermal energy increasing the degree of crystallization.^[12c, 17] Interestingly, HCP exhibited a decreased L_c , L_a , and N indicating the size of the order-layered nanodomain decreased due to the thermal decomposition of NaBH₄.

$$L_{a/c} = \frac{K\lambda}{\beta_{a/c} \cos\theta_{a/c}} \quad \text{Equation (1)}$$

$$N = \frac{L_c + d_{002}}{d_{002}} \quad \text{Equation (2)}$$

Where β is the full width at half-maximum (FWHM) of the XRD peak, λ is the wavelength of the X-ray used ($\lambda_{\text{Mo}} = 0.071$ nm), θ is the position of (002) and (100) peaks in XRD, and the corresponding K values of 0.89 and 1.84 for (002) and (100), respectively.^[18]

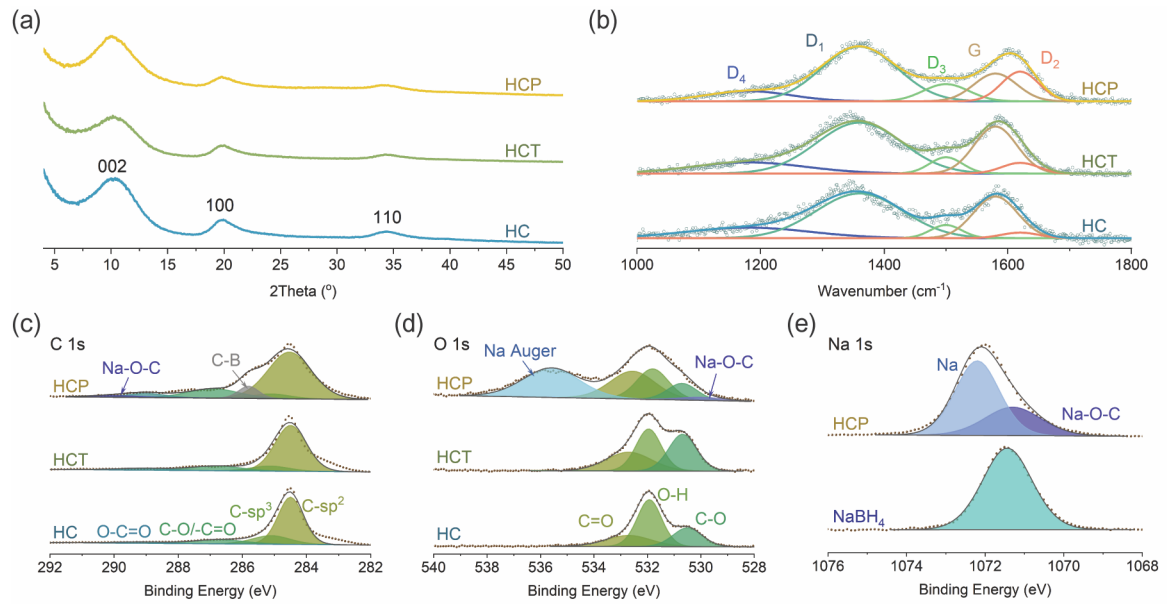


Figure 1 a) XRD patterns, b) Raman spectra, and high resolution XPS c) C 1s, and d) O 1s spectra of HC, HCT, and HCP, and e) comparison of XPS Na 1s spectra of HCP and as-received NaBH₄.

Table 1. Physical parameters of the hard carbon materials

	d_{002} (Å)	L_a (nm)	L_c (nm)	Number of graphene layers (N)	I_D/I_G	A_{D4}/A_G
HC	3.89	3.59	1.09	3.82	1.14	0.71
HCT	3.86	4.04	1.27	4.30	1.07	0.64
HCP	4.01	3.14	1.05	3.62	1.17	0.72

The Raman spectra of HC, HCT and HCP in Figure 1b have two characteristic peaks located at around 1345 and 1585 cm⁻¹, which are attributed to the C–C vibrational mode in the disordered (D-band) and graphitized (G-band) carbon structures, respectively. Thus, the I_D/I_G intensity ratio can provide an insight into the degree of disorder in the hard carbon structure. HCT possessed a lower I_D/I_G ratio compared to that of HC (1.07 vs. 1.14), attributing to the removal of functional groups and the increase in the graphitization by the supplied thermal energy.^[12c] HCP exhibited the highest I_D/I_G (1.16) which can be attributed to the incorporation of sodium/boron into the hard carbon network during the presodiation. In order to better understand the structural evolution during thermal treatment and presodiation, the Raman spectra were deconvoluted into five peaks centering at 1180, 1360, 1500, 1585, and 1620 cm⁻¹ corresponding to D4, D1, D3, G, and D2 bands, respectively.^[12b, 15b] The G band is ascribed to the ideal C–C vibrations in graphitic lattice with E_{2g}-symmetry, while D1 and D2 bands are referred to C–C vibrations in disordered graphitic lattices with A_{1g}- and E_{2g}-symmetries, respectively. The D3 band corresponds to the amorphous carbon and D4 is mainly due to ionic impurities.^[19] Thus, the ratio of carbon bonded to functional groups on the HC surface to the amount bonded to the graphitic layer can be estimated from the area ratio of D4 and G (A_{D4}/A_G). By this estimation, HCT had the lowest A_{D4}/A_G ratio while HCP exhibited the highest A_{D4}/A_G ratio agreeing with the I_D/I_G ratio (Table 1).

X-ray photoelectron spectroscopy (XPS) was conducted to reveal the carbon, oxygen, and sodium electronic states in HC, HCT, and HCP. The high-resolution C 1s spectra in Figure 1c can be resolved into four components with center at 284.5, 285.2, 286.7, and 289.1 eV corresponding to C_{sp2}, C_{sp3}, C–O/C=O, and O–C=O.^[12a] The C_{sp2}:C_{sp3} ratio of HC and HCT are 3.61 and 7.49, respectively, indicating the formation of a highly ordered carbon structure during the thermal treatment. Interestingly, both HC and HCT exhibited a decreasing C_{sp2}:C_{sp3} ratio in the depth profile (Figures S1a and b), suggesting that the oxygen in the inner part cannot be dissociated out of the structure even at high temperatures. Comparing with HC and HCT, HCP exhibited two additional peaks centered at 285.7 and 290.0 eV which can be attributed to C–B^[20] and Na–O–C,^[21] respectively. The boron binding energy shifted from 187.2 and 191.5 eV in NaBH₄ to 187.8 eV in HCP (Figure S1c), which can be assigned to C–B^[22], further affirming that the boron has been doped into the hard carbon structure during the thermal presodiation. The Na–O–C binding is supported with the additional peak at 530.4 eV for HCP in O 1s (Figure 1d) and 1071.2 eV in Na 1s XPS spectra (Figure 1e).^[9a, 14b] Besides Na–O–C, HCP also had one Na 1s XPS peak around 1072.2 eV which can be ascribed to metallic sodium.^[23]

Scanning electron microscopy (SEM) images of the pristine HC, HCT, and HCP (Figure 2a-f, respectively) show similar particle morphology and size (~10–30 µm), indicating that neither thermal treatment nor presodiation causes any noticeable change in particle size. At higher magnification, the surfaces of HC and HCT were smooth while HCP appeared to be textured. This is likely due to the deposition of decomposed products from NaBH₄ on the HCP surface. Furthermore, the scanning transmission electron microscopy with energy dispersive X-ray spectroscopy (STEM-EDX) image reveals strong Na signals, detecting that a significant amount of sodium was deposited on the surface of the HCP particles (Figure 2g). High-resolution transmission electron microscopy (HRTEM) images reveal that all the hard carbon particles consist of curved and randomly orientated graphene layers (Figures S2), which agrees with the “house of cards” model of hard carbon.^[24] Furthermore, the inset selected area electron diffraction (SAED) patterns exhibit dispersed diffraction rings which supports the turbostratic and random stacking of graphene layers. Additionally, the diffraction fringes of the HC, HCT and HCP correspond to an average d_{002} -spacing of 3.87, 3.72, and 3.92 Å, respectively.

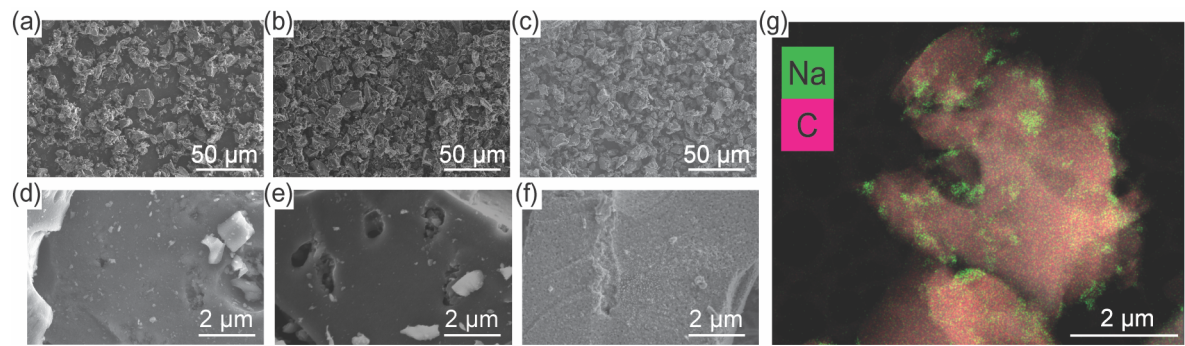


Figure 2. SEM images of a,d) HC, b,e) HCT, and c,f) HCP, respectively, and g) STEM-EDX of HCP

The Na₄(B₁₀H₁₀)(B₁₂H₁₂) (NBH) SSE, with the particle size of ~5–10 µm (Figure S3a), was used as the solid-state electrolyte in this study. The Nyquist plot in Figure S3b suggests that NBH has a room-temperature ionic conductivity of 1.8 mS cm⁻¹ agreeing well with

previous works.^[5, 25] The reduction stability at low potential of NBH was examined by cyclic voltammetry (CV) using a $\text{Na}_9\text{Sn}_4|\text{NBH}|\text{NBH}+\text{stainless-steel}$ cell (Figure S3c). The cell showed a strong reduction peak with an onset around 0 V *vs.* Na/Na^+ that can be attributed to sodium plating on the stainless-steel current collector. On the returning sweep, an oxidation peak that began at around 0.5 V *vs.* Na/Na^+ can be ascribed to stripping of the deposited sodium. More importantly, there was no noticeable reductive current between the OCV and 0 V, which evidently demonstrated that NBH is highly stable at low potential and an interphase layer should not form electrochemically.^[25] It is noteworthy that having an electrochemically stable interface would allow for a larger electrode/electrolyte surface contact area, which is necessary when using a composite electrode to enhance the sodium diffusion kinetics, without reducing the mobile sodium ions inventory.

The effect of physical contact between the HC and SSE on the electrochemical performance was evaluated by assembling different HC:NBH composite (e.g., 100:0, 80:20, 70:30, and 60:40) in a half-cell configuration using Na_9Sn_4 as the counter electrode; the lower HC:NBH ratio in the composite, the larger the electrolyte/electrode contact area is. Galvanostatic (de)sodiation cycling was carried out to study the sodium storage mechanisms. Comparing the potential profiles, 100 wt.% HC exhibited a low potential ‘plateau’ profile while composite HCs had a ‘slope’ followed by low potential ‘plateau’ profile (Figure S4a). This hints different sodium storage mechanism which can be attributed to the lack of physical contact between the SSE and HC for electrochemical reactions. Consequently, the 100 wt.% HC had an ICE of 43.0% while the composite anodes had an ICE of 83.5 to 84.9%. More importantly, the absolute irreversible capacity was consistently around 43–46 mAh g⁻¹ (0.38–0.41 mAh cm⁻²) indicates the HC/SSE interfaces are relatively stable. Although all composite HC exhibited similar capacity at low current density, 70wt.% HC delivered a highest normalized capacity at higher current density (Figure S4b). Thus, an anode composite HC:NBH wt.% ratio of 70:30 was used for this study.

Figure 3a shows the Nyquist plots of the as-assembled HC, HCT and HCP half-cells. All cells showed a high-frequency Z' -axis intercept followed by one semicircle (10^5 – 10^4 Hz), which can be attributed to the NBH resistance and electrode/electrolyte interface resistance, respectively, and a polarization tail.^[26] HCP exhibited a smaller polarization tail in the low-frequency region compared to HC and HCT, which implies that the cell was at a different state-of-charge. This observation indicates that sodium was present within the HCP structure. Nevertheless, using the equivalent circuit (Figure 3a inset), all cells had similar total cell resistances (~ 90 – $100 \Omega\text{cm}^2$), which includes the NBH and interface resistance, at the as-assembled state indicating no significant differences in the interfacial properties between different hard carbon electrodes.

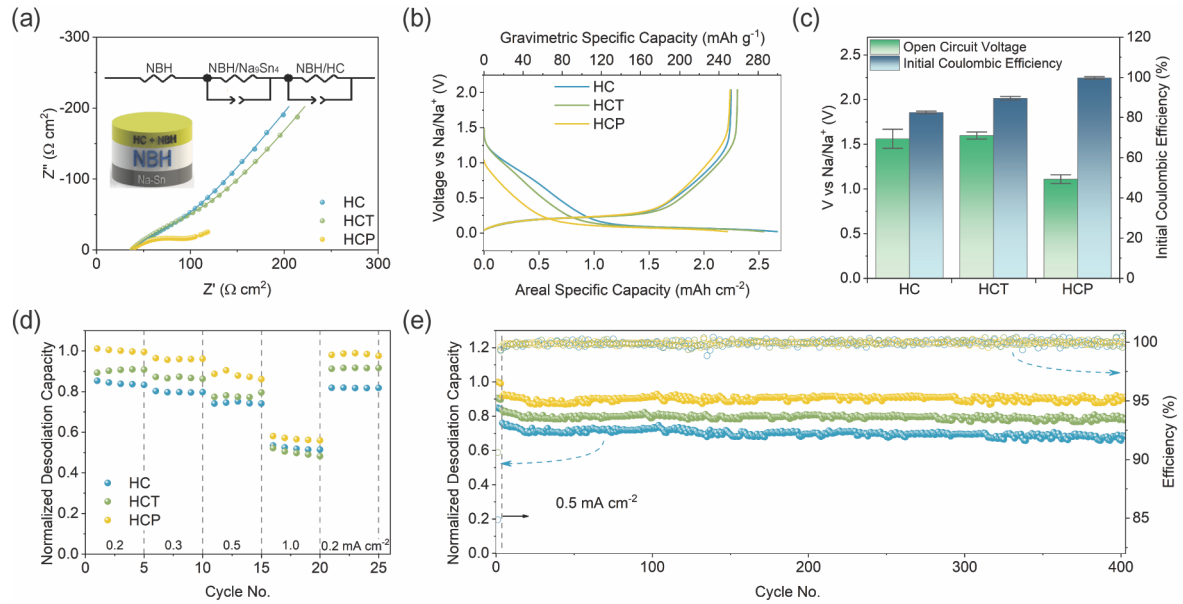


Figure 3 a) Nyquist plot of the pristine HC|NBH|Na₉Sn₄ half-cell, b) potential profile of HC at a current density of 0.2 mA cm⁻², c) OCV and ICE of HCs half-cells, d) potential profile of HCP at different current densities, e) reversible capacity of HCs at different current densities, and f) long-term cycling performance of half-cell at a current density of 0.5 mA cm⁻².

The potential response of the respective HC|NBH|Na₉Sn₄ half-cells (Figure 3b) was like those observed in liquid electrolytes,^[21, 27] with a slope at >0.15 V and a plateau between 0.15–0.02 V vs. Na/Na⁺ during sodiation. This indicates that the HC has a similar sodium storage mechanism in a solid-state battery as in a liquid electrolyte battery. All cells delivered a sodiation capacity of around 260–280 mAh g⁻¹ (or 2.25–2.40 mAh cm⁻²), which is close to the capacity of HC reported in the liquid electrolyte battery, indicating a good utilization of the active material in the composite electrode. Upon desodiation, all cells delivered similar capacities of approximately 245–255 mAh g⁻¹. Accordingly, HCP had the highest ICE of 99.6±0.6%, followed by HCT (89.6±0.9%), then HC (82.5±0.6%). The corresponding dQ/dV profile in the first cycle showed only one pair of distinct (de)sodiation peaks near 0.06 V and 0.26 V vs. Na/Na⁺ (Figure S5a), which can be ascribed to the insertion and removal of sodium from the HC structure. Additionally, HCP had a significantly lower average open-circuit voltage (OCV) of 1.11±0.05 V compared to pristine HC and HCT at 1.56±0.11 and 1.60±0.04 V vs. Na/Na⁺ (Figure 3c), respectively. This affirms that HCP was at different state-of-charge following presodiation. Interestingly, the reversible capacities of HC and HCT in the subsequent cycle were relatively constant (~245–255 mAh g⁻¹) and the Coulombic efficiencies were above 99% after the initial sodium loss during the first cycle. This observation suggests that the initial sodiation involved both reversible and irreversible sodium storage sites and only the reversible ones took part in the electrochemical reaction in subsequent cycles. In order to show that the deposited sodium on HCP is electrochemically active, the Na₉Sn₄||HCP half-cell was desodiated in the initial cycle (Figure S5b). A desodiation capacity of 9.63 mAh g⁻¹ and the subsequent cycle showed a Coulombic efficiency of 89.6%, which is close to HCT's efficiency. Intuitively, the supplemental sodium sources saturate all the irreversible sites in the initial sodiation and, thus, the sodium provided by the counter electrode is almost all

completely reversible. To verify that the improvement of the ICE in HCP is due to the decomposition of NaBH_4 at high temperature, two samples were prepared; (1) HCT were thermally treated again under vacuum (e.g., HCT-T) and (2) HCT was physically mixed with NaBH_4 (HCP-NH). Both HCT-T and HCP-NH did not show significant improvement in the ICE (Figures S5c,d). These further demonstrate that thermal decomposition of NaBH_4 is necessary to effectively nullify Na loss due to the irreversible Na sites present in HC.

The rate performance of HC, HCT and HCP at 0.2, 0.3, 0.5, and 1.0 mA cm^{-2} current densities and the normalized capacity is given in Figure 3d. Accordingly, HCP delivered a higher normalized reversible capacity than HCT and HC at all current densities, which can be attributed to its lower capacity loss in the initial cycle. All cells recovered their initial capacity when the current density returned to 0.2 mA cm^{-2} , indicating that the configuration is tolerant to higher current densities. The lower reversible capacity at higher current density can be attributed to sluggish electrochemical kinetics within the hard carbon and/or at the HC/NBH interface. Nevertheless, the differences in the reversible normalized capacity between different HC samples can be directly ascribed to the different ICE. The sodium storage reversibility of the HC, HCT, and HCP were investigated by repeated cycling at 0.2 mA cm^{-2} for 3 cycles followed by 0.5 mA cm^{-2} for 400 cycles (Figure S6b-d). Although HCP exhibited a lower sodiation capacity of 245 mAh g^{-1} than HC and HCT (290 and 285 mAh g^{-1} , respectively) at 0.2 mA cm^{-2} , all cells had similar desodiation capacity of 245–260 mAh g^{-1} . Figure 3e shows the normalized desodiation capacity the long-term galvanostatic cycling and the HCP cell delivered a higher normalized reversible capacity due to the improved ICE. All cells had minimal capacity fading after 400 cycles at 0.5 mA cm^{-2} and an average Coulombic efficiency of 99.9%, which reflects that (de)sodiation within hard carbon structure is highly reversible.

To study the impact of supplemental sodium ions on the half-cell performance, hard carbons presodiated with excess capacity (e.g., HCP-x where $x = 20, 40$, and 60 mAh/g) were prepared by mixing different amounts of NaBH_4 with HC. The XRD profiles suggest that either no or low wt.% secondary crystallized phase formation (Figure S7a). Furthermore, comparing to HCP with zero excess in Figure 2g, HCP-60 exhibited a significantly stronger distribution of Na signals credited to more sodiation on the HC particles. (Figure 4a). Due to the supplemental sodium, the sodiation capacities from the counter electrode reduced while the desodiation capacities were consistently around 240–260 mAh g^{-1} (Figure S7b). Moreover, the OCV of the assembled cells decreased from 1.11 to 0.80 V vs Na/Na^+ as more excess capacity from NaBH_4 was added to the mixture (Figure 4b). Therefore, the ICE of HCP increases with the amount of NaBH_4 added, while the capacities in the subsequent cycles were recovered to about 240–260 mAh g^{-1} (Figure S7c). The dQ/dV plots of the HCP-x overlapped each other indicating that they exhibit a similar sodium storage mechanism (Figure 4c), as expected. However, the cells exhibited a lower excess capacity than the theoretical capacity provided by the thermal decomposition of NaBH_4 and such deviation increases with more NaBH_4 added. To investigate this, the amount of Na was quantified by titration gas chromatography (TGC).^[27b, 28] The calculated capacity obtained via TGC deviates slightly from the electrochemical excess capacities suggesting formation of sodium compound reducing the active sodium inventory (Figure S7d). The distribution of B and Na on the HCP-60 was verified by electron energy-loss spectroscopy (EELS) elemental mapping (Figure S7e and 4d). More importantly, the EELS

B K edge spectrum (Figure 4e) suggests that the thermal decomposition of NaBH_4 leads to the formation of a Na-B-C compound which has similar bonding as NaB_5C which has low sodium capacity reversibility.^[29] As a result, the excess capacity is lower than the theoretical value. Nevertheless, it is still possible to presodiate the HC with excess capacity by adding more NaBH_4 and, thus, enabling the use of sodium-deficient cathode materials (e.g., $\text{Na}_{2/3}\text{Ni}_{1/3}\text{Mn}_{2/3}\text{O}_2$ ^[30] and $\text{Na}_{0.6}[\text{Li}_{0.2}\text{Mn}_{0.8}]\text{O}_2$ ^[31]) in a full-cell configurations and in full-cell configurations where SEI formation consumes a significant portion of the fixed Na inventory.

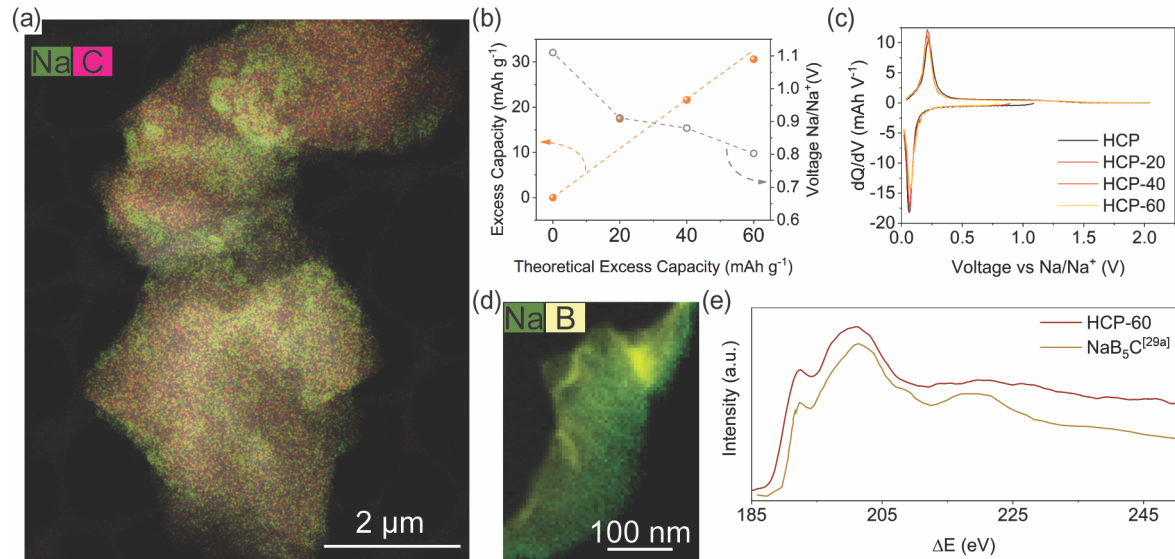


Figure 4 a) STEM-EDS mapping of HCP-60, b) excess capacity and OCV, c) dQ/dV plot of HCP-x, and EELS d) mapping and e) B K edge of HCP-60.

Given the electrochemical stability between HC and SSE, the HC and HCT still possessed an ICE <90% implies there were intrinsic irreversible sites in the structure. This is reflected by the OCV of all cells after one charge-discharge cycle which were around 1.15 V vs. Na/Na^+ , which is significantly lower than in the pristine state, indicating that they were at different state-of-charge. The HC and HCT cells were desodiated with a constant current constant voltage (CCCV) step, but negligible capacity could be recovered even at higher cut-off voltage (Figures S8a,b). This suggests that the irreversible sodium ions were not limited by kinetics but rather were thermodynamically stable and irreversible due to the strong binding energy between the sodium ions and hard carbon. Nyquist plots of the HC, HCT, and HCP cells at the desodiated state during the 20 cycles at 0.2 mA cm^{-2} showed similar resistance, indicating no significant degradation or formation of a resistive interphase that occurred during cycling (Figure S8c). The cyclic voltammograms of HC, HCT, and HCP cells exhibited two redox pairs at 0.65/1.20 and 0.02/0.35 V vs. Na/Na^+ (Figure 5a–c), suggesting that HCs exhibited two-stage sodium storage mechanisms, which agrees well with sodium storage in HC using liquid electrolyte.^[32] It is worthy to note that HC had a strong reduction peak at ~0.65 V, which became weaker in subsequent cycles, while HCT also exhibited such changes but at a reduced scale. Interestingly, the sodium metal on HCP that shifted into the irreversible sites was not detected in the CV, potentially due to the lower pristine OCV and reduction peak overlapped with the OCV, making it less obvious. Similar behavior was also observed in the dQ/dV profiles (Figures S9a–c). Particularly, a weaker reduction peak in the subsequent cycles indicates the

electrochemical reaction in this voltage range became slightly inactive after the initial cycle.

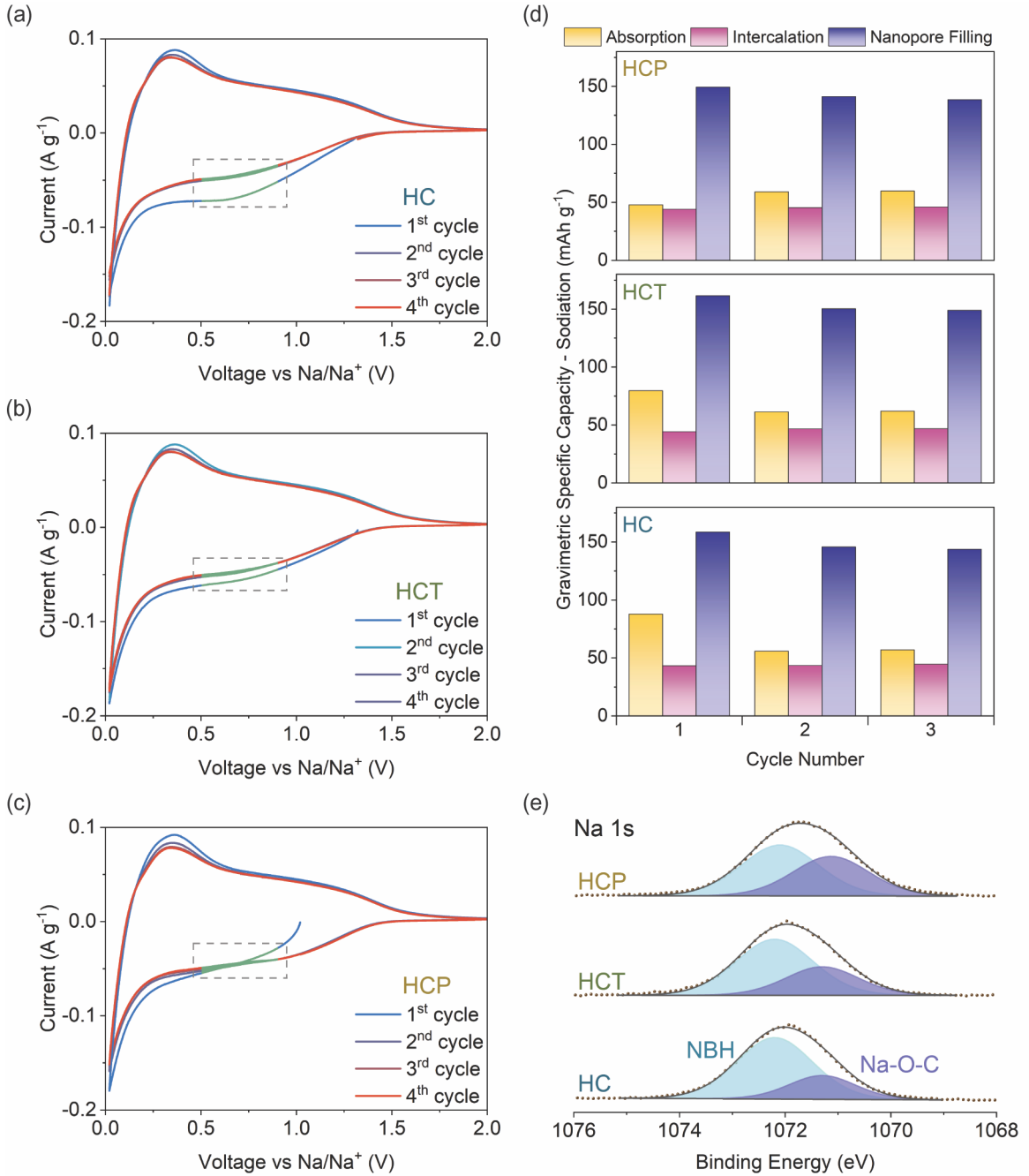


Figure 5 Cyclic voltammogram of a) HC, b) HCT, and c) HCP. d) Initial 3 cycles sodiation capacity according to the sodium storage mechanism. e) High-resolution Na 1s XPS spectra after the first cycle.

To further investigate the irreversible sodium capacity, capacities of the HCs were deconvoluted into the ‘slope’, ‘transition’, and ‘plateau’ capacity regions (Figures S9d–f) according to the “adsorption-intercalation-nanopore filling” mechanism.^[27a] According to this mechanism, the ‘slope’ capacity can be attributed to the pseudo-adsorption and defect-adsorption mechanisms. The defect-adsorption mechanism is associated with a large binding energy between the functional groups and the incoming sodium ions which cannot

be extracted even by a CCCV step.^[12a] There was negligible intercalation and nanopore filling capacity changes during the initial three cycles indicating a good reversibility sodium storage mechanism in all HCs (Figure 5d). Among all, HCP exhibited the least changes in the ‘adsorption’ capacity followed by HCT and HC which coincide with the amount of adsorption sodiation capacity of HCP, HCT, and HC (~47.9, 79.6, 87.9 mAh g⁻¹, respectively) and the observation in cyclic voltammogram. Thus, the majority of the irreversible sodium ions in HC and HCT can be attributed to the low reversibility of the ‘adsorption’ capacity.

The Na 1s XPS spectra of all cells after one galvanostatic cycle can be resolved into two peaks at 1072.3 and 1071.2 eV (Figure 5e), which can be attributed to the sodium in NBH electrolyte and Na–O–C group in the HC electrodes, respectively. The presence of Na–O–C was also reported in *ex-situ* XPS of hard carbon after sodiating to the adsorption capacity.^[11, 21] This observation evidenced that sodium ions that were strongly bound to the oxygen functional groups in hard carbon would lead to irreversible capacity loss. Since intrinsic irreversibility is inevitable due to the structure of HC, presodiation is required to achieve high initial coulomb efficiencies.

The importance of achieving high ICE is further overstated when using a full-cell configuration (AS³iB) consisting of HC (HCT or HCP), NBH, Na_{2.25}Y_{0.25}Zr_{0.75}Cl₆ (NYZC) and NaCrO₂ (NCO) as the anode, SSE, catholyte, and cathode, respectively. Due to the limited sodium ions inventory provided by NCO, any sodium loss in the initial or subsequent cycles will negatively affect the reversible capacity of the cell. **Figure 6a** shows the potential response of the AS³iBs during the first cycle at 1/10 C (1 C = 120 mA g_{NCO}⁻¹). Compared to the potential response of Na₉Sn₄||NCO (Figure S10a,b), the AS³iBs with HC, HCT, and HCP showed an initial ‘slope’ profile, followed by a potential profile that is like the Na₉Sn₄||NCO half-cell in the later stages of charging. Furthermore, the AS³iBs had the ‘hump’ between 1.5 to 2.5 V in the initial cycle dQ/dV plots which is absence in Na₉Sn₄||NCO half-cell (Figure S11a-d). This observation agrees well with the sodiation potential profile of HCs, which consist of slope followed by plateau (Figure 3b). Additionally, the intensity of the ‘hump’ decreased after the initial cycle with the exception for HCP cell indicating the irreversible sodium storage in hard carbon in the initial cycle. Although all cells exhibited similar charge capacities around 115–120 mAh g⁻¹, the discharge capacity of HC, HCT, and HCP were 86, 91, and 102 mAh g⁻¹, respectively. Accordingly, HC, HCT, and HCP AS³iBs exhibited ICEs of 75.2±0.7%, 82.2±1.1%, and 92.0±2.2%, respectively. This trend agrees well with the ICEs of the half-cells. Additionally, HCP had an initial discharge energy density of 294 Wh kg_{NCO}⁻¹ which is higher than HC and HCT (238 and 279 Wh kg_{NCO}⁻¹, respectively). This is due to reduced ‘slope’ capacity in HCP, resulting in a higher average cell voltage and higher ICE.

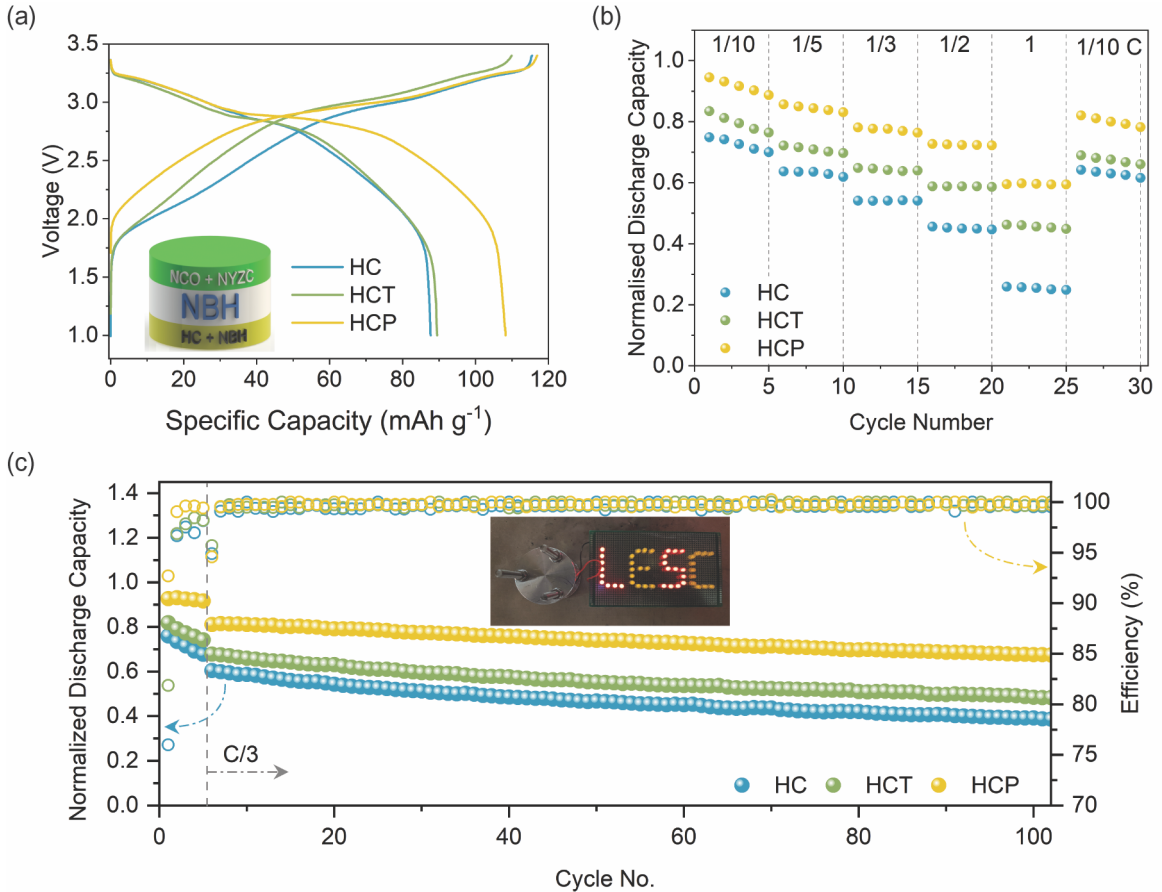


Figure 6 a) Potential response of HCs|NBH|NYZC|NCO AS³iBs in the initial cycle at 1/10 C. b) Reversible discharge capacity at varying current densities. c) Capacity retention of HCs|NBH|NYZC|NCO cell at 1/3 C.

Figure 6b shows the normalized reversible capacities of AS³iBs at different current densities and the potential profiles of cells using HC, HCT, and HCP are depicted in Figure S11. Like the half-cell trend, the HCP delivered the highest reversible capacity compared to HCT and HC. The capacities returned to similar initial capacity when the current density was reduced back to 1/10 C implying that AS³iBs were highly stable at high current densities. It is noteworthy that the Coulombic efficiency of all cells improved to above 98% within the next 4 cycles at 1/10 C indicating a good reversibility of the cells. Thus, the reversible capacity differences are predominantly caused by initial sodium loss in the first cycle.

The reversibility of the AS³iBs were studied by cycling at 1/10 C for 5 cycles, which act as the formation cycles, followed by 100 cycles at a 1/3 C (Figure 6c). HCP delivered a higher initial normalized capacity of 0.92 and 0.81 compared to HC (0.76 and 0.60) and HCT (0.82 and 0.68) at 1/10 and 1/3 C, respectively. It is noteworthy that the HC and HCT cells exhibited a greater increase in overpotential over 100 cycles than that of HCP full-cell (Figure S12). As a result, HC and HCT had a lower capacity retention of 60.1% and 70.8%, respectively, than HCP (82.3%) after 100 cycles at 1/3 C. Thus, presodiation of the anode is one of the promising strategies to achieve high performance all-solid-state sodium-ion batteries.

3. Conclusion

This study demonstrated that HC is a promising anode candidate in AS³iBs. However, the intrinsic irreversible sodium loss in the HC led to low ICE even when paired with an electrochemically stable solid-state electrolyte. This study explored two strategies to improve the ICE: thermal treatment at 1000 °C and presodiation by the thermal decomposition of NaBH₄. Thermal treatment of hard carbon was shown to be effective in increasing crystallinity and the C_{sp2}:C_{sp3} ratio. The thermal decomposition of NaBH₄ produced sodium metal on the surface of the HC particles, which was shown to be necessary to compensate for the intrinsic irreversible sodium storage sites. Consequently, thermally treated HC improved the ICE from 83% to 90% and the presodiated HC achieved an ICE >99%. Additionally, the half-cells exhibited minimal capacity fading after 200 cycles at 0.5 mA cm⁻². More notably, AS³iBs with presodiated HC and NCO as the anode and cathode, respectively, delivered a reversible discharge capacity of 102 mAh g⁻¹ at room temperature and an extremely high ICE of 92%, which is significantly higher than that of HC (75%) and HCT (82%). This work demonstrates significant progress towards enabling practical sodium AS³iBs by utilizing presodiated HC.

4. Experimental

Synthesis of NBH: Stoichiometric amount of Na₂B₁₀H₁₀ and Na₂B₁₂H₁₂ (Boron Specialties LLC) were ball-milled at 500 rpm for 2 h. The as-obtained powder was then dried at 175 °C under vacuum for 48 h. Due to its hydroscopic nature, all operations were conducted in a glovebox with H₂O <1.0 ppm.

Hard carbon preparation: The pristine HC (MSE Supplies LLC) was used as received. To study the thermal treatment effect, HC was thermally treated at 1000 °C for 2 h forming HCT. HCP was synthesized by mixing a proportional amount of NaBH₄ (Sigma-Aldrich) and HC using a mortar and pestle. Then, the mixture was thermally treated at 650 °C for 3 h in sealed quartz ampoule under vacuum. The amount of NaBH₄ added to the HC was calculated according to the capacity loss in the initial cycle.

Material characterization: XRD was conducted using a Bruker X8-ApexII CCD Sealed Tube diffractometer equipped with a molybdenum K α radiation ($\lambda = 0.71$ Å) over a 2 θ range of 5 to 40°. Samples were sealed in a thin-walled capillary tubes to minimize ambient air exposure. Raman spectroscopy was performed using Renishaw inVia Raman Microscope and 532 nm laser source. Due to its air-sensitivity, HCP was sealed on very thin glass slides with Kapton tape in Ar-filled glovebox. XPS was conducted using a Kratos Axis Supra XPS instrument and Al K α radiation. The data was then analyzed using CasaXPS and was calibrated using the C 1s peak at 284.5 eV. Titration gas chromatography was conducted using Agilent Technologies 7890B to quantify the amount of hydrogen and the amount of metallic sodium was calculated according to **Equation 3**. SEM images were acquired by an FEI Scios DualBeam Focused ion beam, equipped with an Everhart–Thornley Detector. TEM was performed on a Talos F200X Scanning/Transmission Electron Microscope at 200 kV. HR-TEM and HAADF images were collected with a Ceta camera. STEM-EDS/EELS was collected with 4 in-column SDD Super-X detectors and Gatan's Enfinium ER (977) spectrometer with UltraFast DualEELS spectrum, respectively.



Electrochemistry characterization: Composite HC electrodes were prepared by homogenizing the HC (or HCT/HCP) and NBH with a mass ratio of 70:30 using a mortar

and pestle. The half-cell configuration using Na_9Sn_4 as the counter electrode was prepared by compacting NBH at 225 MPa. Then, the composite electrode was added on one side and structure was compact again at 225 MPa. Finally, Na_9Sn_4 was added to the other side of the NBH and the cell was compacted again at 225 MPa. For comparison, different HC composite electrodes (with a HC:NBH ratio of 100:0, 80:20, and 60:40) half-cells were prepared by following similar procedures as described earlier but the weight of composite electrodes varies to have 7 mg of active HC to achieve similar capacity. The AS³iB (full-cell) configuration includes the composite HC (HCT or HCP), NBH, and composite NaCrO_2 (NCO) as the anode, electrolyte, and cathode, respectively, with an negative:positive electrode capacity ratio of 1.2. The cathode composite was prepared according to previous work with a NCO:NYZC:C weight ratio 4:5:1.^[33] The AS³iB was compacted with a pressure of 225 MPa. The NCO active material of the electrode was around 6.11 mg cm⁻². All capacities were normalized by the initial sodiation capacity of HCs.

CV and electrochemical impedance spectroscopy (EIS) measurements were conducted using a Solartron S1260 impedance analyzer coupled with a Solartron 1287 potentiostat. EIS was conducted in a frequency between 1 MHz to 0.1 Hz at room temperature and with an applied voltage of 10 mV. The EIS of the cell was recorded after resting the cell for at least 3 h. The galvanostatic cycling of the cell was conducted using a Landt battery cycler. The average ICE and OCV were calculated based on 4 of the similar cells. For the AS³iBs, the cells were cycled between 1 and 3.4 V. The capacities of the AS³iBs were normalized by the weight of the NCO in the cathode composite.

5. Acknowledgement

This work was supported by Shell (Project No.: 2025754) and National Science Foundation through the Partnerships for Innovation (PFI) (Grant No.: 2044465). Electron microscopy was performed at the San Diego Nanotechnology Infrastructure (SDNI) of UCSD, a member of the National Nanotechnology Coordinated Infrastructure, which is supported by the National Science Foundation (Grant No.: ECCS-2025752). X-ray photoelectron spectroscopy was performed using facilities in UC Irvine Materials Research Institute (IMRI), which is supported in part by the National Science Foundation through the UC Irvine Materials Research Science and Engineering Center (Grant No.: DMR-2011967) and National Science Foundation Major Research Instrumentation Program (Grant No.: CHE-1338173). J.A.S. Oh is thankful for post-doctorate fellowship support from the Agency of Science, Technology, and Research (A*STAR).

6. References

- [1] X. Sun, M. Ouyang, H. Hao, *Joule* **2022**, 6, 1738, 1738.
- [2] H. S. Hirsh, Y. Li, D. H. S. Tan, M. Zhang, E. Zhao, Y. S. Meng, *Advanced Energy Materials* **2020**, 10, 2001274.
- [3] a)J. A. S. Oh, L. He, B. Chua, K. Zeng, L. Lu, *Energy Storage Materials* **2021**, 34, 28, 28; b)S. Wenzel, T. Leichtweiss, D. A. Weber, J. Sann, W. G. Zeier, J. Janek, *ACS Appl Mater Interfaces* **2016**, 8, 28216.
- [4] a)L. Duchêne, R. S. Kühnel, E. Stilp, E. Cuervo Reyes, A. Remhof, H. Hagemann, C. Battaglia, *Energy & Environmental Science* **2017**, 10, 2609, 2609; b)L. Duchêne, S. Lunghammer, T. Burankova, W.-C. Liao, J. P. Embs, C. Copéret, H. M. R. Wilkening, A.

Remhof, H. Hagemann, C. Battaglia, *Chemistry of Materials* **2019**, 31, 3449, 3449; c)A. Gigante, L. Duchene, R. Moury, M. Pupier, A. Remhof, H. Hagemann, *ChemSusChem* **2019**, 12, 4832.

[5] L. Duchene, R. S. Kuhnel, D. Rentsch, A. Remhof, H. Hagemann, C. Battaglia, *Chem Commun (Camb)* **2017**, 53, 4195.

[6] a)M. Lao, Y. Zhang, W. Luo, Q. Yan, W. Sun, S. X. Dou, *Adv Mater* **2017**, 29, 1700622, 1700622; b)Z. G. Liu, R. Du, X. X. He, J. C. Wang, Y. Qiao, L. Li, S. L. Chou, *ChemSusChem* **2021**, 14, 3724; c)T. Perveen, M. Siddiq, N. Shahzad, R. Ihsan, A. Ahmad, M. I. Shahzad, *Renewable and Sustainable Energy Reviews* **2020**, 119, 109549.

[7] a)D. A. Stevens, J. R. Dahn, *Journal of The Electrochemical Society* **2000**, 147, 1271; b)E. Irisarri, A. Ponrouch, M. R. Palacin, *Journal of The Electrochemical Society* **2015**, 162, A2476, A2476; c)V. L. Chevrier, G. Ceder, *Journal of The Electrochemical Society* **2011**, 158, A1011.

[8] a)J. Sun, Y. Sun, J. A. S. Oh, Q. Gu, W. Zheng, M. Goh, K. Zeng, Y. Cheng, L. Lu, *Journal of Energy Chemistry* **2021**, 62, 497, 497; b)M. Zhang, Y. Li, F. Wu, Y. Bai, C. Wu, *Nano Energy* **2021**, 82, 105738.

[9] a)X. Liu, Y. Tan, T. Liu, W. Wang, C. Li, J. Lu, Y. Sun, *Advanced Functional Materials* **2019**, 29, 1903795; b)E. de la Llave, V. Borgel, K. J. Park, J. Y. Hwang, Y. K. Sun, P. Hartmann, F. F. Chesneau, D. Aurbach, *ACS Appl Mater Interfaces* **2016**, 8, 1867.

[10] S. Komaba, W. Murata, T. Ishikawa, N. Yabuuchi, T. Ozeki, T. Nakayama, A. Ogata, K. Gotoh, K. Fujiwara, *Advanced Functional Materials* **2011**, 21, 3859, 3859.

[11] E. Memarzadeh Lotfabad, P. Kalisvaart, A. Kohandehghan, D. Karpuzov, D. Mitlin, *J. Mater. Chem. A* **2014**, 2, 19685, 19685.

[12] a)D. Sun, B. Luo, H. Wang, Y. Tang, X. Ji, L. Wang, *Nano Energy* **2019**, 64, 103937; b)X. Dou, I. Hasa, D. Saurel, C. Vaalma, L. Wu, D. Buchholz, D. Bresser, S. Komaba, S. Passerini, *Materials Today* **2019**, 23, 87, 87; c)L. Xiao, H. Lu, Y. Fang, M. L. Sushko, Y. Cao, X. Ai, H. Yang, J. Liu, *Advanced Energy Materials* **2018**, 8, 1703238.

[13] a)D. Dewar, A. M. Glushenkov, *Energy & Environmental Science* **2021**, 14, 1380, 1380; b)K. Zou, W. Deng, P. Cai, X. Deng, B. Wang, C. Liu, J. Li, H. Hou, G. Zou, X. Ji, *Advanced Functional Materials* **2020**, 31, 2005581.

[14] a)M. Liu, J. Zhang, S. Guo, B. Wang, Y. Shen, X. Ai, H. Yang, J. Qian, *ACS Appl Mater Interfaces* **2020**, 12, 17620; b)G. Zheng, Q. Lin, J. Ma, J. Zhang, Y. B. He, X. Tang, F. Kang, W. Lv, Q. H. Yang, *InfoMat* **2021**, 3, 1445, 1445.

[15] a)S. Qiu, L. Xiao, M. L. Sushko, K. S. Han, Y. Shao, M. Yan, X. Liang, L. Mai, J. Feng, Y. Cao, X. Ai, H. Yang, J. Liu, *Advanced Energy Materials* **2017**, 7, 1700403; b)S. Alvin, D. Yoon, C. Chandra, H. S. Cahyadi, J.-H. Park, W. Chang, K. Y. Chung, J. Kim, *Carbon* **2019**, 145, 67, 67.

[16] Y. Cao, L. Xiao, M. L. Sushko, W. Wang, B. Schwenzer, J. Xiao, Z. Nie, L. V. Saraf, Z. Yang, J. Liu, *Nano Lett* **2012**, 12, 3783.

[17] H. D. Asfaw, C. W. Tai, M. Valvo, R. Younesi, *Materials Today Energy* **2020**, 18, 100505.

[18] a)Z.-l. Zhang, R. Brydson, Z. Aslam, S. Reddy, A. Brown, A. Westwood, B. Rand, *Carbon* **2011**, 49, 5049, 5049; b)H. Lu, F. Ai, Y. Jia, C. Tang, X. Zhang, Y. Huang, H. Yang, Y. Cao, *Small* **2018**, 14, e1802694.

[19] A. Sadezky, H. Muckenhuber, H. Grothe, R. Niessner, U. Pöschl, *Carbon* **2005**, 43, 1731, 1731.

[20] Y. Chang, X. Sun, M. Ma, C. Mu, P. Li, L. Li, M. Li, A. Nie, J. Xiang, Z. Zhao, J. He, F. Wen, Z. Liu, Y. Tian, *Nano Energy* **2020**, 75, 104947.

[21] Y. Li, Y.-S. Hu, M.-M. Titirici, L. Chen, X. Huang, *Advanced Energy Materials* **2016**, 6, 1600659.

[22] T. Shirasaki, A. Derré, M. Ménétrier, A. Tressaud, S. Flandrois, *Carbon* **2000**, 38, 1461, 1461.

[23] A. Barrie, F. J. Street, *Journal of Electron Spectroscopy and Related Phenomena* **1975**, 7, 1, 1.

[24] Y. Liu, J. S. Xue, T. Zheng, J. R. Dahn, *Carbon* **1996**, 34, 193, 193.

[25] G. Deysher, Y. T. Chen, B. Sayahpour, S. W. Lin, S. Y. Ham, P. Ridley, A. Cronk, E. A. Wu, D. H. S. Tan, J. M. Doux, J. A. S. Oh, J. Jang, L. H. B. Nguyen, Y. S. Meng, *ACS Appl Mater Interfaces* **2022**, 14, 47706.

[26] J. T. S. Irvine, D. C. Sinclair, A. R. West, *Advanced Materials* **1990**, 2, 132, 132.

[27] a)M. Yuan, B. Cao, H. Liu, C. Meng, J. Wu, S. Zhang, A. Li, X. Chen, H. Song, *Chemistry of Materials* **2022**, 34, 3489, 3489; b)H. S. Hirsh, B. Sayahpour, A. Shen, W. Li, B. Lu, E. Zhao, M. Zhang, Y. S. Meng, *Energy Storage Materials* **2021**, 42, 78, 78.

[28] C. Fang, J. Li, M. Zhang, Y. Zhang, F. Yang, J. Z. Lee, M. H. Lee, J. Alvarado, M. A. Schroeder, Y. Yang, B. Lu, N. Williams, M. Ceja, L. Yang, M. Cai, J. Gu, K. Xu, X. Wang, Y. S. Meng, *Nature* **2019**, 572, 511.

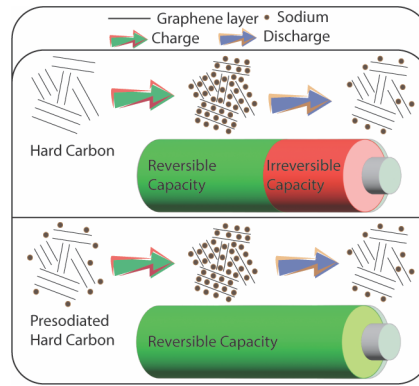
[29] a)K. Hofmann, R. Gruehn, B. Albert, *Zeitschrift für anorganische und allgemeine Chemie* **2002**, 628, 2691, 2691; b)M. R. Shabetai, Vol. Ph.D, University of New Orleans, 2022.

[30] Y. Zhang, M. Wu, J. Ma, G. Wei, Y. Ling, R. Zhang, Y. Huang, *ACS Cent Sci* **2020**, 6, 232.

[31] Q. Liu, Z. Hu, W. Li, C. Zou, H. Jin, S. Wang, S. Chou, S.-X. Dou, *Energy & Environmental Science* **2021**, 14, 158, 158.

[32] a)K.-l. Hong, L. Qie, R. Zeng, Z.-q. Yi, W. Zhang, D. Wang, W. Yin, C. Wu, Q.-j. Fan, W.-x. Zhang, Y.-h. Huang, *Journal of Materials Chemistry A* **2014**, 2, 12733; b)N. Sun, Z. Guan, Y. Liu, Y. Cao, Q. Zhu, H. Liu, Z. Wang, P. Zhang, B. Xu, *Advanced Energy Materials* **2019**, 9, 1901351.

[33] E. A. Wu, S. Banerjee, H. Tang, P. M. Richardson, J. M. Doux, J. Qi, Z. Zhu, A. Grenier, Y. Li, E. Zhao, G. Deysher, E. Sebti, H. Nguyen, R. Stephens, G. Verbist, K. W. Chapman, R. J. Clement, A. Banerjee, Y. S. Meng, S. P. Ong, *Nat Commun* **2021**, 12, 1256.



The oxygen groups in hard carbon are the intrinsic irreversible sodium storage sites leading to loss of sodium inventory which negatively impacting the energy density of batteries. Hard carbon is presodiated by decomposing sodium-containing precursors thermally. This supplemental sodium populates the irreversible sites improving the initial Coulombic efficiency and the energy density of all-solid-state sodium ion batteries.